Electric field switching of altermagnetic spin-splitting in multiferroic skyrmions

Gui Wang[1†], Yuhang Li[2†], Bin Li[3†], Xianzhe Chen[1*], Jianting Dong[4], Weizhao Chen[5], Xiaobing Chen[5], Naifu Zheng[5], Maosen Guo[6], Aomei Tong[6], Hua Bai[7], Hongrui Zhang[8], Yifan Gao[1], Kaiwen Shen[1], Jiangyuan Zhu[1], Jiahao Han[9], Yingfen Wei[1], Hao Jiang[1], Xumeng Zhang[1], Ming Wang[1], Kebiao Xu[6], Wu Shi[3], Pengfei Wang[10,14], Jia Zhang[4], Qihang Liu[5,11], Cheng Song[7], Qi Liu[1], Xincheng Xie[12,13,14], and Ming Liu[1]

[1] *Frontier Institute of Chip and System, State Key Laboratory of Integrated Chips and Systems, Zhangjiang Fudan International Innovation Center, Fudan University, Shanghai 200433, China*

[2] *School of Physics, Nankai University, Tianjin 300071, China*

[3] *State Key Laboratory of Surface Physics and Institute for Nanoelectronic Devices and Quantum Computing, Fudan University, Shanghai 200433, China*

[4] *School of Physics and Wuhan National High Magnetic Field Center, Huazhong University of Science and Technology, Wuhan 430074, China*

[5] *China Quantum Science Center of Guangdong-Hong Kong-Macao Greater Bay Area (Guangdong), Shenzhen 518045, China*

[7] *Key Laboratory of Advanced Materials (MOE), School of Materials Science and Engineering, Tsinghua University, Beijing 100084, China*

[8] *Ningbo Institute of Materials Technology & Engineering, Chinese Academy of Sciences, Ningbo 315201, China*

[9] *Center for Science and Innovation in Spintronics, Tohoku University, 2-1-1 Katahira, 980-8577 Sendai, Japan*

[10] *CAS Key Laboratory of Microscale Magnetic Resonance and School of Physical Sciences, University of Science and Technology of China, Hefei 230026, China*

[11] *State Key laboratory of quantum functional materials, Department of Physics, and Guangdong Basic Research Center of Excellence for Quantum Science, Southern University of Science and Technology (SUSTech), Shenzhen 518055, China*

[12] *Interdisciplinary Center for Theoretical Physics and Information Sciences (ICTPIS), Fudan University, Shanghai 200433, China*

[13] *International Center for Quantum Materials, Peking University, Beijing 100871, China*

[14] *Hefei National Laboratory, Hefei 230088, China*

Magnetic skyrmions are localized magnetic structures that retain their shape and stability over time, thanks to their topological nature[1–10]. Recent theoretical and experimental progress has laid the groundwork for understanding magnetic skyrmions characterized by negligible net magnetization and ultrafast dynamics[11–18]. Notably, skyrmions emerging in materials with altermagnetism[19–27], a novel magnetic phase featuring lifted Kramers degeneracy—have remained unreported until now. In this study, we demonstrate that $BiFeO_3$, a multiferroic renowned for its strong coupling between ferroelectricity and magnetism[28–31],

---

[*] E-mail: chenxianzhe@fudan.edu.cn

1

can transit from a spin cycloid to a Néel-type skyrmion under antidamping spin-orbit torque at room temperature. Strikingly, the altermagnetic spin splitting within BiFeO$_3$ skyrmion can be reversed through the application of an electric field, revealed via the Circular photogalvanic effect. This quasiparticle, which possesses a neutral topological charge, holds substantial promise for diverse applications—most notably, enabling the development of unconventional computing systems with low power consumption and magnetoelectric controllability.

In conventional antiferromagnets[32–35] with collinear moment alignments, the connection between magnetic sublattices relies on translation (τ) or parity ($\mathcal{P}$) operations, resulting in Kramers degeneracy, despite a disruption of pure time-reversal ($\mathcal{T}$) symmetry. In contrast, altermagnets connect their magnetic sublattices through rotation transformation, rather than τ or $\mathcal{P}$ operations, which leads to a compensated alternating spin density in real space and simultaneously, nonrelativistic spin-momentum locking in reciprocal space[20,36,37]. The unique alternating lifting of Kramers degeneracy in altermagnets gives rise to time-reversal symmetry-breaking magneto-responses[38] that are typically absent in conventional collinear antiferromagnets, e.g. anomalous Hall effect[19,21,25,39], tunneling magnetoresistance[40,41] and magnetic spin Hall effect[23,42]. In this article, we demonstrate the existence of altermagnetism in skyrmion phase of multiferroic BiFeO$_3$ (BFO). BFO is a model multiferroic that exhibits both antiferromagnetism (Néel temperature of ~ 643 K) and ferroelectricity (Curie temperature $\sim 1,100$ K and a large polarization ~ 90 μC cm^{-2}) as well as intrinsic magnetoelectric coupling of these co-existing order parameters[23,42]. In the bulk, BFO possesses a rhombohedrally distorted perovskite structure in which a spin cycloid with a period length of ~ 62 nm is formed due to the intrinsic Dzyaloshinskii-Moriya interaction (DMI)[43,44]. In turn, BFO exhibits outstanding magnetoelectric properties that have made it the focus of numerous studies hoping to utilize it as a platform to achieve low-energy memory and logic devices[29,30,45,46].

Figure 1a presents the crystal structure of BFO, highlighting the positions of the Bi, Fe, and O atoms, represented by red, yellow, and purple spheres, respectively. The ferroelectric polarization, denoted as $\mathbf{P}$, is aligned along the [111] direction. This polarization is accompanied by an octahedral rotation of the oxygen atoms, giving rise to an inhomogeneous DMI between the second nearest neighboring spins[44] [$(\mathbf{D}_2 \times \mathbf{e}_{ij}) \cdot (\mathbf{S}_i \times \mathbf{S}_j)$, where $\mathbf{e}_{ij}$ is the vector connecting $\mathbf{S}_i$ and $\mathbf{S}_j$]. This DMI facilitates the formation of spin cycloid structure in BFO ground state and is crucial for the formation of the magnetic skyrmion. In addition, a homogeneous DMI [$\mathbf{D}_1 \cdot (\mathbf{S}_i \times \mathbf{S}_j)$] also exists between nearest neighboring spins, which introduces a canting angle between neighboring spins and thus leads to a small net magnetization[44,47]. Since the combined parity and time-reversal ($\mathcal{PT}$) symmetry as well as spinor ($\mathcal{U}$) symmetry are explicitly breaking in BFO lattice due to the octahedral rotation of the oxygen atoms, BFO is anticipated to exhibit spin splitting in momentum space ($\mathbf{K}$-space). To reveal the altermagnetism of BFO, the spin-polarized energy band structures of BFO are calculated in $\mathbf{K}$-space without considering the spin-orbit coupling, where the ferroelectric polarization is directed along [111] (Fig. 1b). This splitting arises from the alternating crystal environment for the magnetic sublattice due to the octahedral rota-

tion, leading to nonrelativistic momentum-dependent electronic states for spin-up and spin-down carriers, and thus indicating that BFO is an altermagnet (Data Fig. 1), which is consistent with previous studies[48,49]. The spin splitting of BFO is ~ 0.1 eV, in the same order as typical altermagnets e.g. Mn_5Si_3[22,25], MnF_2[50]. In contrast, Figure 1c shows the spin-splitting dispersion when the ferroelectric polarization points along the $[1\bar{1}1]$ direction, where the polarity of spin-splitting flip sign. The reversed splitting features observed in this configuration highlight the potential for controlling altermagnetism through the ferroelectricity of BFO.

The magnetic ground state of BFO is a spin cycloid as illustrated in Fig. 2a (inset). In this configuration, the antiferromagnetic moments rotate within a plane that is formed with ferroelectric polarization $\mathbf{P}$ and the propagation direction $\mathbf{q}$, which is also perpendicular to the direction of $\mathbf{D}_2$ (Extended Data Fig. 2). However, the spin cycloid state is susceptible to external perturbations, particularly to the spin torque from spin currents[51,52]. When spin currents generated by the spin Hall effect[53] are injected into BFO, they interact with the existing magnetic structure[54–56], leading to a transition from the cycloid state to a skyrmion state (Extended Data Fig. 3). This transition is facilitated by the unique interplay between the spin currents and the DMI. The spin current introduces an anti-damping torque, which disturbs the spins and hence drives BFO into a high energy magnetic state. This state subsequently relaxes into the skyrmion configuration owing to the stabilizing influence of DMI[57–59]. Figure 2a presents a calculated phase diagram that delineates the boundaries among the cycloid, stripes and skyrmion states. The x-axis of the diagram represents the injected current density, while the y-axis indicates the strength of the inhomogeneous DMI ($\mathbf{D}_2$). The diagram clearly shows that a sufficient spin current can induce the transition from the spin cycloid to the skyrmion state. On the other hand, scanning nitrogen-vacancy microscopy (SNVM) in full-B scanning mode is employed to characterize the magnetic structure in BFO. The experimental setup is illustrated in Fig. 2b, where a SOC layer utilized to generate spin current is deposited on the BFO film. The SNVM for imaging is further placed atop of the system. Figure 2c features magnetic domain imaging of the spin cycloid in BFO, where the propagation direction $\mathbf{q}$ corresponds to the ferroelectric polarization $\mathbf{P}$ across different ferroelectric domains, showing strong magnetoelectric coupling in the BFO ground state (Extended Data Fig. 4). In the same region, another magnetic domain image is taken following the injection of a current density of 1.3×10^7 A/cm^2 in SOC (Pt) layer as shown in Fig. 2d. In addition to coexisting non-topological magnetic texture displayed in the bottom, the topological spin textures with radius of ~ 150 nm are clearly observed as highlighted by red circles. Figure 2e summarizes the observed topological states in this region as a function of applied electric current density. The critical switching current density for SrIrO$_3$ (SIO)-capped devices ($J_c = 3.5 \times 10^6$ A/cm^2) is significantly lower than that of Pt-capped devices ($J_c = 1 \times 10^7$ A/cm^2), demonstrating a 3-fold reduction that directly correlates with the giant spin Hall angle of SIO compared to Pt (Extended Data Fig. 5). It should also be noted that the ferroelectric domains remain unchanged under current injection in SOC layer (Extended Data Fig. 6).

Next, we delve into the detailed analysis of the skyrmion phase in BFO. This in principle can be revealed by the spatial distribution of the stray field uniquely bound to the magnetic spin texture. In Fig. 2f, we detect the three-dimensional stray field map $\mathbf{B}(x,y)$ of a single skyrmion ob-

tained through scanning NV probe at the sample surface. The two-dot feature is strikingly distinct compared to the cycloid state. To elucidate the nature of this magnetic structure, we reconstruct the stray field components along the x, y and z directions, as shown in Figs. 2(g-i). In Fig. 2g, the B_x component illustrates the spatial variation of the magnetic field along the horizontal axis, showcasing regions of both positive (red) and negative (blue) stray fields. Similarly, Figure 2h depicts the B_y component, while Fig. 2i shows the B_z component, which reflects the vertical behavior of the skyrmion's stray field in relation to the sample surface. The distinct distributions of these components highlight the complexity of the stray field of this topological spin texture and its dependence on spatial orientation. In general, the stray field exhibits four bright spots in B_x component, three bright spots in B_y component while two bright spots in B_z component. Figures. 2(k-m) display simulated stray field distributions of three corresponding components for a skyrmion with the $\mathbf{D}_1$ direction aligned along the [100] axis (Fig. 2j). Notably, these simulated stray field distributions agree remarkably well with the experimental results shown in Figs. 2(g-i), which confirms the presence of skyrmions in our experiments. Because the skyrmion size is smaller than the ferroelectric domain width, the zigzag pattern in Fig.2c does not interfere with the stablization of this altermagnetism. Moreover, since the direction of the DMI can be modulated through the ferroelectric polarization, this can subsequently give rise to distinct magnetic configurations of skyrmions (Extended Data Fig. 7), which depends on $\mathbf{D}_1$ direction.

Distinct skyrmion configurations are stabilized by different ferroelectric polarization ($\mathbf{P}$) orientations in BFO. Given that $\mathbf{P}$ can be deterministically switched by an electric field, we further investigate direct electric-field control of the skyrmion phase, as demonstrated in Fig. 3. Experimental SNVM images capture the transformation of spin textures upon the electric field switching. Under a negative 300 kV/cm gate electric field, the local polarization rotates toward [$\bar{1}$11] axis, as evidenced by the spin cycloid phase, stabilizing a distinct skyrmion lattice configuration, where the direction of $\mathbf{D}_1$ is along [110] axis (Fig. 3a). When an equivalent positive electric field is applied, $\mathbf{P}$ switches to [111] axis, and the cycloid wave vector rotates 90° in-plane (Extended Data Fig. 8). Simultaneously, the skyrmion pattern flips to the configuration with the DMI along the [1$\bar{1}$0] axis (Fig. 3b). This transformation indicates that the electric field can control the ferroelectric polarization in BFO, which in turns switches the skyrmion domains. The experimental observations are reproduced by our simulations with varying $\mathbf{D}_1$ (Figs. 3a-h). The simulated stray field maps (left panels in Figs. 3c-h) show near-perfect agreement with measured SNVM data (right panels in Figs. 3c-h). Next, we check the cyclability of the electric-field control of BFO skyrmion. SNVM images after successive $\mathbf{P}$ switches show reproducible flipping of the in-plane stray field components (Figs. 3i-m), while skyrmion size and stability remain unchanged. Notably, the entire process is driven solely by the electric field, without the assistance of an additional magnetic field or spin current. Fundamentally, the direct electric control of DMI orientation via polarization switching affirms an intrinsic magnetoelectric coupling. This reversible and non-volatile control of BFO skyrmion demonstrates a voltage-gated pathway to manipulate altermagnetic topological texture with ultralow power consumption.

The central advance lies in our ability to probe spin splitting through optical excitation and manipulate it with electric field. In contrast to spin cycloid, skyrmion exhibits non-vanish spin-

4

splitting analogous to collinear state[60]. To access this spin-polarized band structure, we employ the circular photogalvanic effect (CPGE), a helicity-dependent optoelectronic response that maps spin-polarized carrier excitation to probe the spin splitting in BFO. As illustrated in Fig. 4a, circularly polarized light generates a photocurrent whose sign depends on the photon helicity. Light of a given helicity excites charges with spin up, while of opposite helicity excites charges with spin down[61–64]. The left panels in Figs. 4b and c schematically illustrate the two-dimensional projections of the electron energy bands on the $k_x - k_y$ plane when the polarization direction $\mathbf{P}$ is along [111] and [11$\bar{1}$], respectively. The electrodes are placed along the y-axis direction and are at a $45°$ angle to the polarization direction. The two right panels in Figs. 4b and c show the different skyrmion configurations after applying positive and negative electric fields, where the skyrmion domains are controlled via the polarization switch of BFO. Crucially, we reveal the spin splitting of BFO skyrmion in Fig. 4d, which also link the CPGE response to the ferroelectric polarization state. A quarter-wave plate is used to change the light polarization. As shown in the top panel of Fig. 4d, under a positive gate electric field of 300 kV/cm, we observe a clear sinusoidal modulation of photocurrent as a function of the quarter-wave plate angle (φ). As φ is varied, the light polarization gradually changes from linear to elliptical, and eventually to circular. The maximum current magnitude is recorded at $\varphi = 45°$ for left-handed ($\circlearrowleft$) circular polarization and $\varphi = 135°$ for right-handed ($\circlearrowright$) circular polarization. In the bottom panel of Fig. 4d, upon a negative electric field of identical magnitude, $\mathbf{P}$ is switched towards [11$\bar{1}$]. The spin photocurrent polarity flips from positive to negative for the same photon helicity.

To further reveal the spatially resolved spin-splitting in BFO, we map the photocurrent generated under $\circlearrowleft$ and $\circlearrowright$ circularly polarized light across the sample surface and extract the net spin photocurrent ($I_{\text{CPGE}} = I_\sigma^-(\varphi = 135°) - I_\sigma^+(\varphi = 45°)$). As shown in Fig. 4e, I_{CPGE} exhibits a pronounced, reversible dependence on the applied electric fields, forming a well-defined electrical hysteresis loop at room temperature. The polarity of the I_{CPGE} switches sharply with ferroelectric polarization reversal, indicating tight coupling between the altermagnetic spin-splitting and the ferroelectric state. Insets display representative I_{CPGE} mappings after applying different electric fields (marked by purple asterisks), reflecting the optical spin current response behavior during the electric field switching process. We compare the spatially averaged I_{CPGE} in both the pristine spin cycloid[65] and the induced skyrmion phases under alternatively applied positive/negative electric field (Extended Data Fig. 9). The spin photocurrent from cycloid state exhibits a finite but unidirectional positive signal regardless of field polarity—consistent with the gyrotropy from crystal symmetry or canted moments[65], while the counterpart from skyrmion phase displays a robust antisymmetric dependence on the electric field direction. This polarity reversal originates from momentum-space spin splitting unique to real-space Berry curvature from skyrmion topology. This enables efficient helicity-dependent carrier excitation, whereas the cycloid's fully compensated Néel order suppresses such splitting. Thus, the observation of an electrically switchable, hysteretic spin photocurrent provides compelling evidence of the altermagnetic spin splitting within BFO skyrmions, which can also be reversed through the application of an electric field.

In summary, we have revealed the altermagnetism and its electric-field switch in the multiferroic BFO at room temperature, which is highly pursued theoretically[66–70]. Under anti-damping

spin-orbit torque, spin cycloid in BFO is transformed to skyrmion. BFO skyrmion exhibits non-vanishing altermagnetic spin splitting, as evidenced by our CPGE measurement, where the sign of the spin photocurrent can be reversed via electric field. These deepen our understanding of skyrmion behavior within altermagnets and showcase the potential of these topological structures for future applications in magnetic devices. For example, the electric-field switch of spin splitting in skyrmion has the potential to enable low-energy spintronic devices with minimal stray fields.

Note added—During our submission, we noted a relevant work[64]. Song *et. al.*, broke new ground by demonstrating electrical switching of non-relativistic spin polarization in a p-wave magnet (NiI_2) via the circular photogalvanic effect (CPGE). NiI_2 is a p-wave magnet, whose spin polarizations at $+k$ and $-k$ are opposite, connected by $\mathcal{T}\tau$ symmetry (time reversal followed by fractional translation). In contrast, for altermagnets, the spin polarization at the $+k$ and $-k$ states are the same, connected by $\mathcal{T}U$ symmetry (time reversal followed by spin reversal). We achieved electric-field switching of g-wave altermagnet $BiFeO_3$ at room temperature.
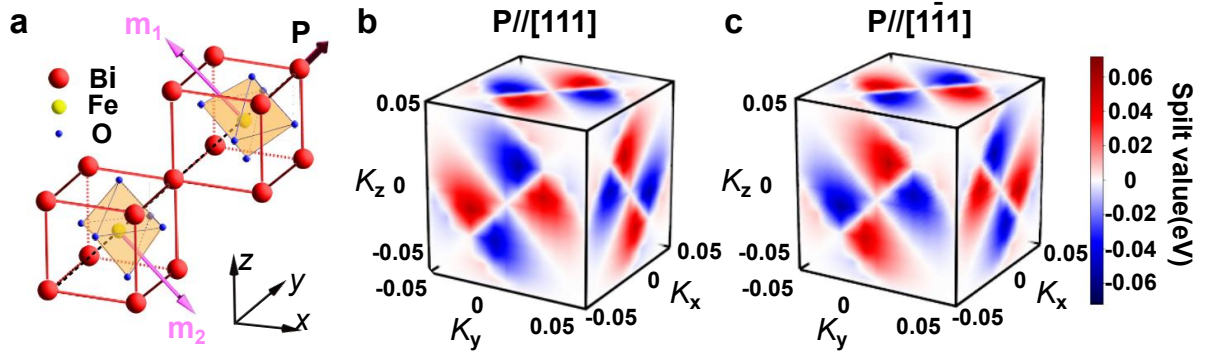
Figure 1: Concept of magnetoelectric altermagnet. a, Crystal structure of BFO, with Bi atoms in red, Fe atoms in yellow, and O atoms in purple. The illustration shows the ferroelectric polarization P along the [111] direction and the octahedral rotation of oxygen, which induces a homogeneous DMI (D_1) parallel to the polarization as well as an inhomogeneous DMI (D_2); the magnetic moments within the unit cell exhibit antiferromagnetic arrangement. **b, c,** Spin-splitting energy dispersion of BFO. The splitting energy value is calculated for the highest band below the Fermi energy, revealing the spin-polarized band structure in K-space. The ferroelectric polarizations are along [111] (**b**) and [1$\bar{1}$1] (**c**) axis, respectively.
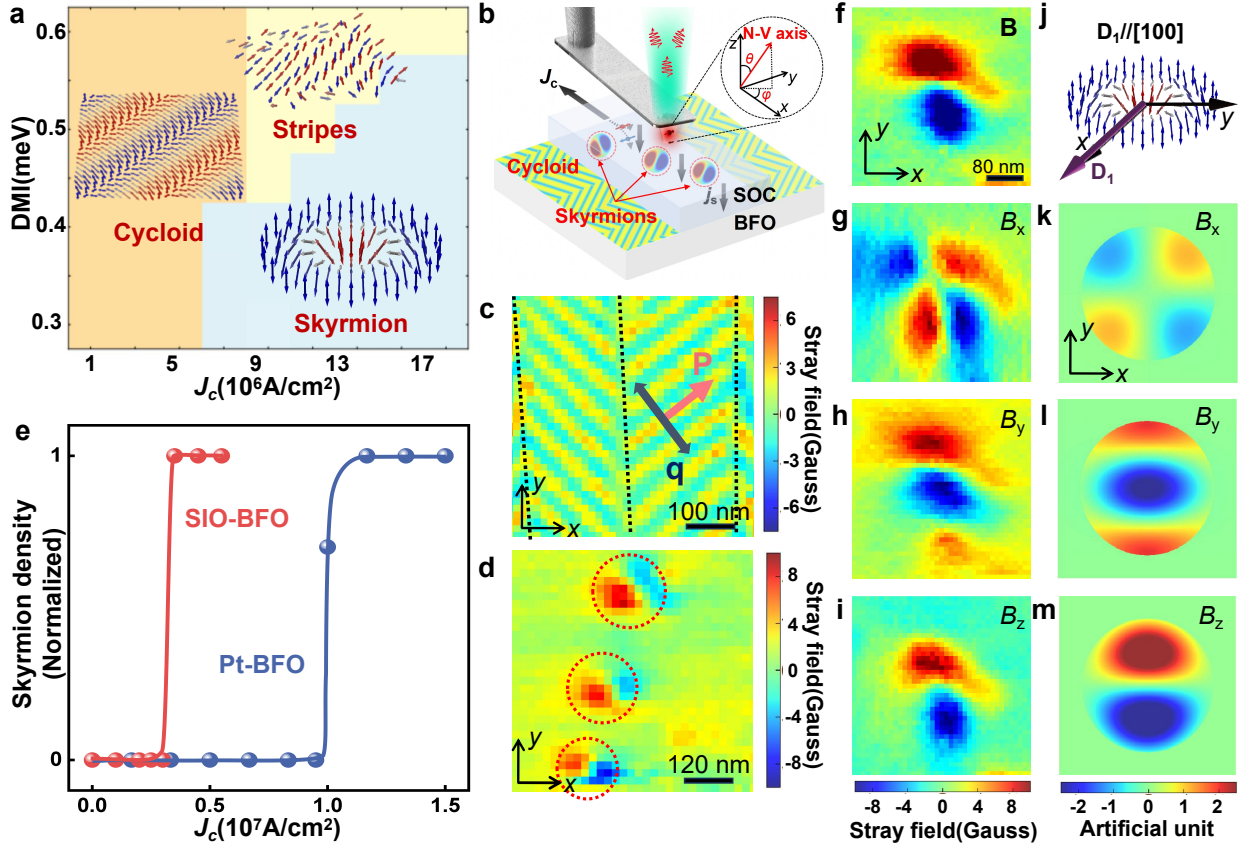
Figure 2: Magnetic structures and phase transition in BFO under spin current injection.
a, Calculated phase diagram versus DMI and injected current densities J_c. Insets schematically illustrate the spin cycloid ground state (left), magnetic stripes (top right), and skyrmion (bottom right). **b,** Schematic of the experimental setup. The SOC layer is deposited on the BFO film and the scan nitrogen vacancy microscope (SNVM) is placed atop for imaging. A spin current J_s, generated via the spin Hall effect in the SOC layer, is injected into BFO, which triggers a phase transition from the cycloid state to the skyrmion. The directions of the SNVM axis and the sample structure (including the SOC layer and the BFO layer) are labeled in the figure. **c,** Magnetic domain image of the spin cycloid in BFO. Red and black arrows in (**c**) indicate the polarization direction **P** and the propagating direction **q**, respectively, within a single domain. Black dashed lines indicate the domain boundaries. **d,** Image of skyrmions (highlighted in red circles) after injecting a current of 1.3×10^7 A/cm^2 through the SOC layer. The scale bar is 100 nm in (**c**) while 120 nm in (**d**). **e,** Normalized skyrmion number per μm^2 versus applied current density I for two different top electrodes SIO/BFO (red) and Pt/BFO (blue). **f,** Normalized three-dimensional stray field map $\mathbf{B}(x,y)$ of a single skyrmion, obtained using SNVM on the sample surface, with x and y representing in-plane coordinates. In our experiment, the x-axis direction points along [100] while the direction points along [010]. **g-i,** Reconstructed stray field components along the x-axis (**g**), y-axis (**h**), and z-axis (**i**) directions based on panel (**f**). **j,** Simulated configuration of the skyrmion, with the homogeneous DMI ($\mathbf{D}_1$) direction aligned along the [100] direction. **k-m,** Simulated stray field distributions of the skyrmion in (**f**) along the x-axis (**k**), y-axis (**l**), and z-axis (**m**) directions. A one-to-one correspondence is observed between panels (**g-i**) and (**k-m**), confirming the presence of skyrmions. All experiments are conducted at room temperature.

8
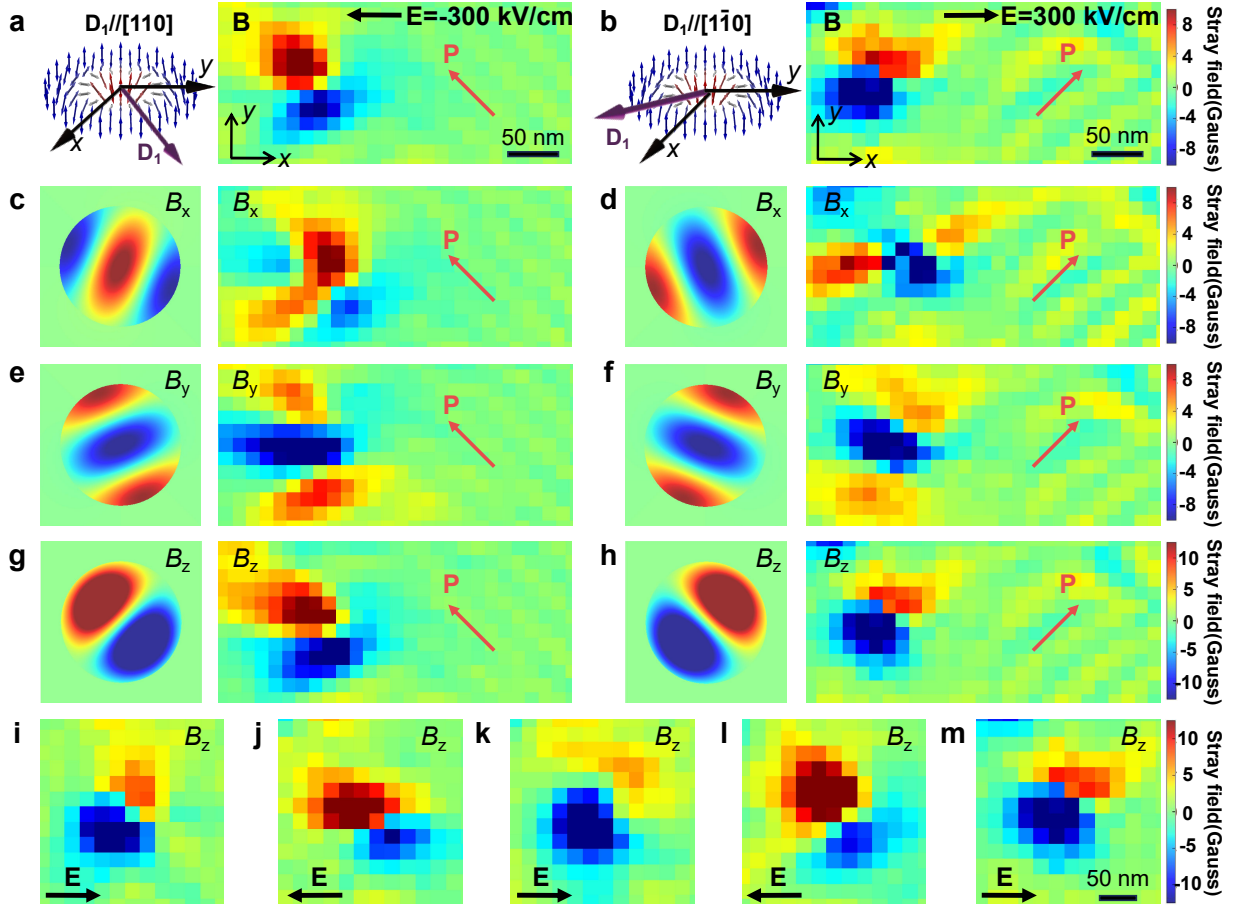
Figure 3: Electric field manipulation of skyrmions. a,b Left panels: Schematics of skyrmion with $\mathbf{D_1}$ along [110] (**a**) and [1$\bar{1}$0] (**b**) directions. Right panels: SNVM image of one skyrmion under E= -300 kV/cm (**a**) and E= 300 kV/cm (**b**), where corresponding polarization **P** aligns perpendicularly along [110] (**a**) and [$\bar{1}$10] (**b**). The comparison between simulated (left panels) and reconstructed stray field (right panels) along x-axis (**c,d**), y-axis (**e,f**), and z-axis (**g,h**) directions for corresponding skyrmions are shown below in (**c,e,g**) [based on panel (**a**)] and (**d,f,h**) [based on panel (**b**)]. Red and indigo arrows indicate the directions of **P** and $\mathbf{D_1}$, respectively. **i-m,** SNVM image represented by reconstructed stray field along z-axis after five consecutive electric field switching. The scale bar is 50 nm inlength.

9
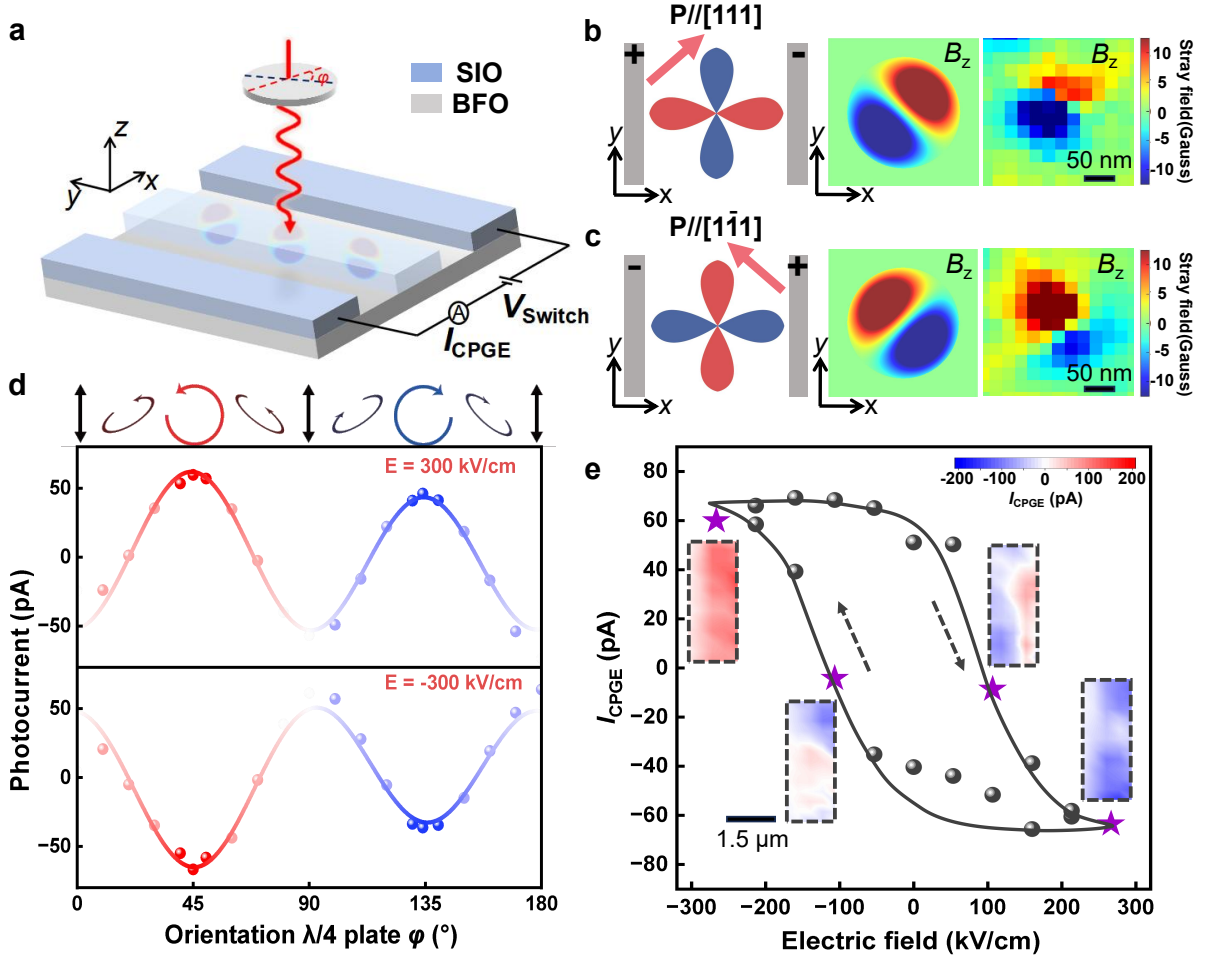
Figure 4: Electric-field switch of spin splitting, probed via the circular photogalvanic effect.
a, Schematics of photocurrent measurement. The spin photocurrent I_{CPGE} is generated from the circular photogalvanic effect under illumination of a 405 nm circularly polarized light. The voltage V_{Switch} is applied to induce an electric field for switching the ferroelectric polarization. **b, c,** Left panels schematically illustrate the two-dimensional projections of the electron energy bands on k_x-k_y plane when the polarization direction is along [111] and [1$\bar{1}$1]. The electrodes are placed along the y-axis direction and are at a 45° angle to the polarization direction. Right panels in (**b**) and (**c**) show the skyrmion configurations after applying positive and negative electric fields to switch the polarization orientation of BFO. **d,** Photocurrent as a function of $\lambda/4$ plate orientation measured with electrodes aligned along y-axis. Left and right -handed circular polarizations are represented as ↻ and ↺. **e,** Responses of the net spin photocurrent (I_{CPGE}) to electric-field modulation in skyrmion state within BFO. Insets display the mappings of I_{CPGE} under the corresponding electric field of the purple asterisks.

10

References

1. Yu, X. *et al.* Real-space observation of a two-dimensional skyrmion crystal. *Nature* **465**, 901–904 (2010).

2. Jiang, W. *et al.* Blowing magnetic skyrmion bubbles. *Science* **349**, 283–286 (2015).

3. Jiang, W. *et al.* Direct observation of the skyrmion Hall effect. *Nat. Phys.* **13**, 162–169 (2017).

4. Woo, S. *et al.* Observation of room-temperature magnetic skyrmions and their current-driven dynamics in ultrathin metallic ferromagnets. *Nat. Mater.* **15**, 501–506 (2016).

5. Boulle, O. *et al.* Room-temperature chiral magnetic skyrmions in ultrathin magnetic nanostructures. *Nat. Nanotechnol.* **11**, 449–454 (2016).

6. Litzius, K. *et al.* Skyrmion Hall effect revealed by direct time-resolved X-ray microscopy. *Nat. Phys.* **13**, 170–175 (2017).

7. Tokura, Y. & Kanazawa, N. Magnetic Skyrmion Materials. *Chemical Reviews* **121**, 2857–2897 (2021).

8. Fert, A., Reyren, N. & Cros, V. Magnetic skyrmions: advances in physics and potential applications. *Nat. Rev. Mater.* **2**, 17031 (2017).

9. Liu, C. *et al.* Magnetic skyrmions above room temperature in a van der waals ferromagnet Fe_3GaTe_2. *Adv. Mater.* **36**, 2311022 (2024).

10. Zhang, C. *et al.* Room-temperature magnetic skyrmions and large topological hall effect in chromium telluride engineered by self-intercalation. *Adv. Mater.* **35**, 2205967 (2023).

11. Barker, J. & Tretiakov, O. A. Static and dynamical properties of antiferromagnetic skyrmions in the presence of applied current and temperature. *Phys. Rev. Lett.* **116**, 147203 (2016).

12. Zhang, X., Zhou, Y. & Ezawa, M. Antiferromagnetic skyrmion: stability, creation and manipulation. *Sci Rep* **6**, 24795 (2016).

13. Gao, S. *et al.* Fractional antiferromagnetic skyrmion lattice induced by anisotropic couplings. *Nature* **586**, 37–41 (2020).

14. Jani, H. *et al.* Antiferromagnetic half-skyrmions and bimerons at room temperature. *Nature* **590**, 74–79 (2021).

15. Legrand, W. *et al.* Room-temperature stabilization of antiferromagnetic skyrmions in synthetic antiferromagnets. *Nat. Mater.* **19**, 34–42 (2020).

16. Amin, O. *et al.* Antiferromagnetic half-skyrmions electrically generated and controlled at room temperature. *Nat. Nanotechnol.* **18**, 849–853 (2023).

17. Pham, V. T. *et al.* Fast current-induced skyrmion motion in synthetic antiferromagnets. *Science* **384**, 307–312 (2024).

18. Vélez, S. *et al.* Current-driven dynamics and ratchet effect of skyrmion bubbles in a ferrimagnetic insulator. *Nat. Nanotechnol.* **17**, 834–841 (2022).

19. Šmejkal, L., González-Hernández, R., Jungwirth, T. & Sinova, J. Crystal time-reversal symmetry breaking and spontaneous Hall effect in collinear antiferromagnets. *Sci. Adv.* **6**, eaaz8809 (2020).

20. Šmejkal, L., Sinova, J. & Jungwirth, T. Emerging research landscape of altermagnetism. *Phys. Rev. X* **12**, 040501 (2022).

21. Feng, Z. *et al.* An anomalous Hall effect in altermagnetic ruthenium dioxide. *Nat. Electron.* **5**, 735–743 (2022).

22. Krempaskỳ, J. *et al.* Altermagnetic lifting of Kramers spin degeneracy. *Nature* **626**, 517–522 (2024).

23. Bai, H. *et al.* Observation of spin splitting torque in a collinear antiferromagnet RuO_2. *Phys. Rev. Lett.* **128**, 197202 (2022).

24. Chen, X. *et al.* Control of spin current and antiferromagnetic moments via topological surface state. *Nat. Electron.* **5**, 574–578 (2022).

25. Han, L. *et al.* Electrical 180 switching of Néel vector in spin-splitting antiferromagnet. *Sci. Adv.* **10**, eadn0479 (2024).

26. Šmejkal, L. *et al.* Chiral magnons in altermagnetic RuO_2. *Phys. Rev. Lett.* **131**, 256703 (2023).

27. Jungwirth, T., Fernandes, R. M., Sinova, J. & Smejkal, L. Altermagnets and beyond: Nodal magnetically-ordered phases (2024). URL https://arxiv.org/abs/2409.10034. arXiv:2409.10034.

28. Wang, J. *et al.* Epitaxial $BiFeO_3$ multiferroic thin film heterostructures. *Science* **299**, 1719–1722 (2003).

29. Chu, Y.-H. *et al.* Electric-field control of local ferromagnetism using a magnetoelectric multiferroic. *Nature Mater.* **7**, 478 (2008).

30. Heron, J. *et al.* Deterministic switching of ferromagnetism at room temperature using an electric field. *Nature* **516**, 370–373 (2014).

31. Gross, I. *et al.* Real-space imaging of non-collinear antiferromagnetic order with a single-spin magnetometer. *Nature* **549**, 252–256 (2017).

32. Wadley, P. *et al.* Electrical switching of an antiferromagnet. *Science* **351**, 587–590 (2016).

33. Wadley, P. *et al.* Current polarity-dependent manipulation of antiferromagnetic domains. *Nat. Nanotechnol.* **13**, 362–365 (2018).

34. Chen, X. Z. *et al.* Antidamping-torque-induced switching in biaxial antiferromagnetic insulators. *Phys. Rev. Lett.* **120**, 207204 (2018).

35. Zheng, D. *et al.* High-efficiency magnon-mediated magnetization switching in all-oxide heterostructures with perpendicular magnetic anisotropy. *Adv. Mater.* **34**, 2203038 (2022).

36. Šmejkal, L., Sinova, J. & Jungwirth, T. Beyond conventional ferromagnetism and antiferromagnetism: A phase with nonrelativistic spin and crystal rotation symmetry. *Phys. Rev. X* **12**, 031042 (2022).

37. Šmejkal, L., Mokrousov, Y., Yan, B. & MacDonald, A. H. Topological antiferromagnetic spintronics. *Nat. Phys* **14**, 242–251 (2018).

38. Amin, O. J. *et al.* Nanoscale imaging and control of altermagnetism in mnte. *Nature* **636**, 348–353 (2024).

39. Reichlova, H. *et al.* Observation of a spontaneous anomalous Hall response in the Mn_5Si_3 d-wave altermagnet candidate. *Nat. Commun.* **15**, 4961 (2024).

40. Chen, X. *et al.* Octupole-driven magnetoresistance in an antiferromagnetic tunnel junction. *Nature* **613**, 490–495 (2023).

41. Shao, D.-F., Zhang, S.-H., Li, M., Eom, C.-B. & Tsymbal, E. Y. Spin-neutral currents for spintronics. *Nat. Commun.* **12**, 7061 (2021).

42. Bose, A. *et al.* Tilted spin current generated by the collinear antiferromagnet ruthenium dioxide. *Nat. Electron.* **5**, 267–274 (2022).

43. Ederer, C. & Spaldin, N. A. Weak ferromagnetism and magnetoelectric coupling in bismuth ferrite. *Phys. Rev. B* **71**, 060401(R) (2005).

44. Rahmedov, D., Wang, D., Íñiguez, J. & Bellaiche, L. Magnetic Cycloid of $BiFeO_3$ from Atomistic Simulations. *Phys. Rev. Lett.* **109**, 037207 (2012).

45. Huang, X. *et al.* Manipulating chiral spin transport with ferroelectric polarization. *Nat. Mater.* 1–7 (2024).

46. Chai, Y. *et al.* Voltage control of multiferroic magnon torque for reconfigurable logic-in-memory. *Nat. Commun.* **15**, 5975 (2024).

47. Albrecht, D. *et al.* Ferromagnetism in multiferroic $BiFeO_3$ films: A first-principles-based study. *Phys. Rev. B* **81**, 140401 (2010).

48. Bernardini, F., Fiebig, M. & Cano, A. Ruddlesden–popper and perovskite phases as a material platform for altermagnetism. *J. Appl. Phys.* **137** (2025).

49. Šmejkal, L. Altermagnetic multiferroics and altermagnetoelectric effect (2024). URL https://arxiv.org/abs/2411.19928. arXiv:2411.19928.

50. Bhowal, S. & Spaldin, N. A. Ferroically Ordered Magnetic Octupoles in d-Wave Altermagnets. *Phys. Rev. X* **14**, 011019 (2024).

51. Miron, I. M. *et al.* Perpendicular switching of a single ferromagnetic layer induced by in-plane current injection. *Nature* **476**, 189–193 (2011).

52. Liu, L. *et al.* Spin-torque switching with the giant spin Hall effect of tantalum. *Science* **336**, 555–558 (2012).

53. Hoffmann, A. Spin Hall effects in metals. *IEEE Trans. Magn.* **49**, 5172–5193 (2013).

54. Han, J. *et al.* Birefringence-like spin transport via linearly polarized antiferromagnetic magnons. *Nat. Nanotechnol.* **15**, 563–568 (2020).

55. Han, J., Cheng, R., Liu, L., Ohno, H. & Fukami, S. Coherent antiferromagnetic spintronics. *Nat. Mater.* **22**, 684–695 (2023).

56. Yoon, J.-Y. *et al.* Handedness anomaly in a non-collinear antiferromagnet under spin–orbit torque. *Nat. Mater.* **22**, 1106–1113 (2023).

57. Li, Z. *et al.* Multiferroic skyrmions in $BiFeO_3$. *Phys. Rev. Res.* **5**, 043109 (2023).

58. Ojha, S. K. *et al.* Morphogenesis of spin cycloids in a noncollinear antiferromagnet. *Proc. Natl. Acad. Sci.* **122**, e2423298122 (2025).

59. Chaudron, A. *et al.* Electric-field-induced multiferroic topological solitons. *Nat. Mater.* **23**, 905–911 (2024).

60. Jin, Z., Zeng, Z., Cao, Y. & Yan, P. Skyrmion Hall Effect in Altermagnets. *Phys. Rev. Lett.* **133**, 196701 (2024).

61. Ganichev, S. D. & Prettl, W. Spin photocurrents in quantum wells. *Journal of physics: Condensed matter* **15**, R935 (2003).

62. McIver, J., Hsieh, D., Steinberg, H., Jarillo-Herrero, P. & Gedik, N. Control over topological insulator photocurrents with light polarization. *Nat. Nanotechnol.* **7**, 96–100 (2012).

63. Duan, S. *et al.* Berry curvature dipole generation and helicity-to-spin conversion at symmetry-mismatched heterointerfaces. *Nat. Nanotechnol.* **18**, 867–874 (2023).

64. Song, Q. *et al.* Electrical switching of a p-wave magnet. *Nature* **642**, 64–70 (2025).

65. Knoche, D. S., Steimecke, M., Yun, Y., Mühlenbein, L. & Bhatnagar, A. Anomalous circular bulk photovoltaic effect in $BiFeO_3$ thin films with stripe-domain pattern. *Nat. Commun.* **12**, 282 (2021).

66. Zhang, R.-W. *et al.* Predictable gate-field control of spin in altermagnets with spin-layer coupling. *Phys. Rev. Lett.* **133**, 056401 (2024).

67. Gu, M. *et al.* Ferroelectric switchable altermagnetism. *Phys. Rev. Lett.* **134**, 106802 (2025).

68. Duan, X. *et al.* Antiferroelectric altermagnets: Antiferroelectricity alters magnets. *Phys. Rev. Lett.* **134**, 106801 (2025).

69. Chen, Y., Liu, X., Lu, H.-Z. & Xie, X. Electrical switching of altermagnetism. *Phys. Rev. Lett.* **135**, 016701 (2025).

70. Song, Q. *et al.* Evidence for a single-layer van der waals multiferroic. *Nature* **602**, 601–605 (2022).

71. Dovzhenko, Y. *et al.* Magnetostatic twists in room-temperature skyrmions explored by nitrogen-vacancy center spin texture reconstruction. *Nat. Commun.* **9**, 2712 (2018).

72. Tan, A. K. C. *et al.* Revealing emergent magnetic charge in an antiferromagnet with diamond quantum magnetometry. *Nat. Mater.* **23**, 205–211 (2024).

Methods
Sample and device fabrication
The epitaxial thin-film BFO in this study was grown by pulsed laser deposition using a KrF excimer laser ($\lambda = 248nm$) on an orthorhombic DyScO$_3$ (110) single-crystal substrate. For SIO/BFO heterostructure, a 40 nm BFO layer was grown at a substrate temperature of 800 °C and an oxygen partial pressure of 0.15 mbar, followed by the growth of a 20 nm SIO layer at 650 °C under oxygen partial pressure of 0.15 mbar. After the growth, the sample was cooled to room temperature in an oxygen environment of 300 mbar at a cooling rate of 20 °C/min. For Pt/BFO devices, after the growth of BFO layer at identical conditions, we fabricatd the devices using photolithography. Afterwards, the Pt layer of 10 nm were deposited by magnetron sputtering.

Scanning NV magnetometry
Scanning-NV magnetometry was performed under ambient conditions with commercial all-diamond scanning probe tips containing single NV defects (SNVM, CIQTEK). The tip was integrated into a tuning-fork based atomic force microscope (AFM) combined with a confocal microscope optimized for single NV defect spectroscopy. Magnetic fields emanating from the sample are detected by recording the Zeeman shift of the NV defect's electronic spin sublevels through optical detection of the electron spin resonance. Experiments were performed with a NV-to-sample distance of approximately 50 nm and a bias magnetic field of 2 mT applied along the NV quantization axis which is at an angle of $\theta_{NV} \approx 54.7°$ with respect to the surface normal.

Photocurrent measurement
Photocurrent measurement was conducted using a home-built confocal microscope (Extended

Data Fig. 10). A 405 nm solid-state laser (CNI Optoelectronics Technology Co., Ltd.) was used as the excitation source. The laser power was attenuated to 520 μW using a density filter and the laser spot (diameter <2 μm) was focused on the sample at normal incidence using a $\times 50$ Olympus objective (0.5 NA). The polarization state of the 405 nm laser was controlled by rotating a quarter-wave plate to switch between left-handed ($\varphi = 45°$) and right-handed ($\varphi = 135°$) circular polarization. Photocurrent mapping was carried out by scanning the laser spot across the sample using a two-axis galvanometer. A chopper (Sine Scientific Instruments Co., Ltd.) modulated the light at 133 Hz to facilitate lock-in detection. The photocurrent signal was amplified by an SR570 current preamplifier (Stanford Research Systems) and collected using an SR830 lock-in amplifier (Stanford Research Systems). The ferroelectric polarity of the BFO sample was switched by applying a poling voltage through a Keithley 2400 source meter (Tektronix, Inc.). All photocurrent measurements presented in the main text were performed at room temperature under ambient conditions.

Magnetic simulation
The Heisenberg spin Hamiltonian of BFO has the form[44,45]

$$H = J \sum_{\langle ij \rangle} \mathbf{S}_i \cdot \mathbf{S}_j + \sum_{\langle ij \rangle} \mathbf{D}_1 \cdot \mathbf{S}_i \times \mathbf{S}_j + \sum_{\langle ij \rangle'} (\mathbf{D}_2 \times \mathbf{e}_{ij}) \cdot (\mathbf{S}_i \times \mathbf{S}_j) + K \sum_i (\mathbf{S}_i \cdot \mathbf{e})^2, \quad (1)$$

where $\mathbf{S}_{i,j}$ represents the unit spin vector at site i,j. The first term is the exchange interaction with strength J. The second and third terms are the homogeneous and inhomogeneous DMI with vectors $\mathbf{D}_1$ and $\mathbf{D}_2$, respectively, representing the DMI strength and direction. The fourth term denotes the uniaxial magnetic anisotropy with strength K along the direction $\mathbf{e}$. The sum $\langle ij \rangle$ and $\langle ij \rangle'$ runs over nearest and next-nearest neighboring, where $\mathbf{e}_{ij}$ is a unit vector connecting next-nearest neighboring sites. In BFO, the Fe atoms are arranged almost uniformly at the center of the unit cell with the lattice constant $a_0 = 0.4$ nm. The specific parameters for BFO are taken as $J = 5.2$ meV, homogeneous DMI $D_1 = 0.05$ meV along [110] direction, inhomogeneous DMI $D_2 = 0.3$ meV along [111] direction, and anisotropy $K = -0.05$ meV along [111] direction. In particular, we consider a cubic lattice of system size $L_x = 100a_0$, $L_y = 100a_0$, $L_z = 2a_0$ with periodic boundary conditions along all three spatial directions.

The magnetic ground state is obtained by numerically minimizing the Hamiltonian in Eq. 1 using a custom Python implementation. This confirms a spin cycloid ground state propagating along [$\bar{1}$10] direction, in agreement with the SNVM image in Fig. 2c. Moreover, the presence of homogeneous DMI ($D_1 = 0.05$meV) introduces a small canting between antiparallel neighboring spins, which hence results in a weak magnetization. On the other hand, we also minimize the Hamiltonian by using the steepest descent method from a designed magnetic state. The result affirms the existence of Néel type skyrmion in BFO (Extended Data Fig. 3).

The transition from spin cycloid to skyrmion can then be unveiled by solving the Landau-Lifshitz-Gilbert-Slonczewski equation[12]

$$\frac{d\mathbf{S}_i}{dt} = -\gamma \mathbf{S}_i \times \mathbf{H}_{eff} + \lambda \mathbf{S}_i \times \frac{d\mathbf{S}_i}{dt} + \xi \mathbf{S}_i \times \mathbf{p} \times \mathbf{S}_i, \quad (2)$$

where $\mathbf{H}_{eff} = \partial H/\partial \mathbf{S}_i$ is the effective magnetic field, γ is the gyromagnetic ratio, λ is the Gilbert damping parameter. The third term represents the Slonczewski spin-transfer torque arising from applied current with $\mathbf{p}$ the torque direction. The torque magnitude ξ is proportional to the applied current density J_c via the relation $\xi = \nu J_c$, where ν represents the spin-torque efficiency. To nucleate a skyrmion, we applied a 10ps current pulse to the spin cycloid ground state. Following the pulse, the system is allowed to relax sufficiently to a steady state using an enhanced damping constant of $\lambda = 0.2$. In these simulations, the spin torque efficiency is taken as $\nu = 10^3 \mathrm{A}^{-1}$, and the magnitude of the inhomogeneous DMI (D_2) varies from 0.3meV to 0.6meV. To further determine the final magnetic state, we examine the spin distribution along with the Néel order topological charge defined as $Q = \sum_i \mathbf{L}_i \cdot \partial_x \mathbf{L}_i \times \partial_y \mathbf{L}_i / 4\pi$, where $\mathbf{L}_i = (\mathbf{S}_i^A - \mathbf{S}_i^B)/2$ is the local Néel vector at site i. As shown in Fig. 2a, we identify three different regions on the $D_2 - J_c$ plane agreeing with the experimental observations. The snapshots for the spin configuration during the nucleation under two different torque $J_c = 1.0 \times 10^6 \mathrm{A} \cdot \mathrm{cm}^{-2}$ and $J_c = 1.1 \times 10^7 \mathrm{A} \cdot \mathrm{cm}^{-2}$ are presented in Extended Data Fig. 11.

Stray field simulation

The stray field in antiferromagnetic materials is generally vanishing because of the antiparallel magnetic moments. Fortunately, in BFO, the neighboring magnetic moments are slightly canted owning to $\mathbf{D}_1$, leading to a unique spatial-dependent stray field that can be detected by the NV center (Extended Data Fig. 12). This stray field is mathematically connected to the canted magnetic moment through the relation[71,72]

$$\mathbf{B}(\mathbf{r}, d) = -\frac{\mu_0 M_s}{2} \begin{pmatrix} -\alpha_z(d,t) * \partial_x^2, & -\alpha_z(d,t) * \partial_y \partial_x, & \alpha_{xy}(d,t) * \partial_x \\ -\alpha_z(d,t) * \partial_y \partial_x, & -\alpha_z(d,t) * \partial_y^2, & \alpha_{xy}(d,t) * \partial_y \\ \alpha_{xy}(d,t) * \partial_x, & \alpha_{xy}(d,t) * \partial_y, & \alpha_z(d,t) * \nabla^2 \end{pmatrix} \begin{pmatrix} m_x(\mathbf{r}) \\ m_y(\mathbf{r}) \\ m_z(\mathbf{r}) \end{pmatrix}, \quad (3)$$

where t is the thickness of BFO, d is the distance between the NV center and the BFO, $\mathbf{r} = (x, y)$ is the spatial coordinate. In the limit of $t \ll d$, the spatial resolution functions $\alpha_{xy}(d,t) = 1/2\pi \cdot td/(d^2 + r^2)^{3/2}$ and $\alpha_z(d,t) = 1/2\pi \cdot t/(d^2 + r^2)^{1/2}$.

The typical expression for a Néel-type antiferromagnetic skyrmion reads

$$\mathbf{L}(\mathbf{r}) = \left(\sin\theta(\mathbf{r})\cos\phi(\mathbf{r}), \quad \sin\theta(\mathbf{r})\sin\phi(\mathbf{r}), \quad \cos\theta(\mathbf{r}) \right), \quad (4)$$

where $\phi(\mathbf{r}) = \arctan y/x$, and $\theta(\mathbf{r}) = \pi r/R$ when $r \leq R$, while $\theta(\mathbf{r}) = \pi$ when others with R the skyrmion size. In the presence of $\mathbf{D}_1$[47], the small net magnetization due to the canting of neighboring magnetic moments is $\mathbf{M}(\mathbf{r}) = \mathbf{D}_1 \times \mathbf{L}(\mathbf{r})$ (Extended Data Fig. 12). In our simulations (Figs. 2 and 3), the skyrmion size $R = 1.5$. The Antiferroelectricity in BiFeO3 Thin Films and the distance between NV center and the sample are taken as $d = 2$, $t = 0.05d$, respectively.

BFO band calculation

The first principles calculations are performed by using the Vienna ab initio simulation package (VASP) with the projector augmented wave (PAW) pseudopotential and the generalized gradient approximation (GGA) exchange-correlation potential. For self-consistency calculation, the plane-

wave kinetic energy cutoff is set to be 600 eV and the total energy convergence criterion is less than 10^{-7} eV by sampling Brillouin zone with a k-point mesh of $8 \times 8 \times 8$.

The lattice constant and atom positions of BFO have been fully relaxed until the Hellmann-Feynman forces on each atom are less than 10^{-3} eV/Å, leading to a pseudo-cubic structure with $a = b = c = 7.997$ Å, and $\alpha = \beta = 90.6°$, $\gamma = 89.3°$. All the calculations are conducted in the absence of spin-orbit coupling, which results in collinear G-type antiferromagnetic order with zero magnetic moment. The ferroelectric polarization of BFO is evaluated to be 106 μC/cm^2 based on Berry phase method, consistent with previous first-principles calculation results.

Author contributions
X.C. supervised this study. G.W., H.B., Y.G. and K.S. carried out the synthesis of heterostructures and fabricated the devices. G.W., M.G., A.T. carried out the NV-imaging measurements. G.W., B.L., Y.G. carried out the CPGE measurements. Y.L., J.D., W.C., X.C., N. Z., J.Z. and X.X. performed the theoretical calculations. H.Z., J.Z., J.H., Y.W., H.J., X.Z., M.W., K.X., W.S., P.W., Q.L., C.S., Q.L. and M.L. gave suggestions on the experiments. All authors discussed the results and prepared the manuscript.


Competing interests
The authors declare no competing interests.

Additional information
Correspondence and requests for materials should be addressed to X.C.. Reprints and permissions information is available at http://www.nature.com/reprints.
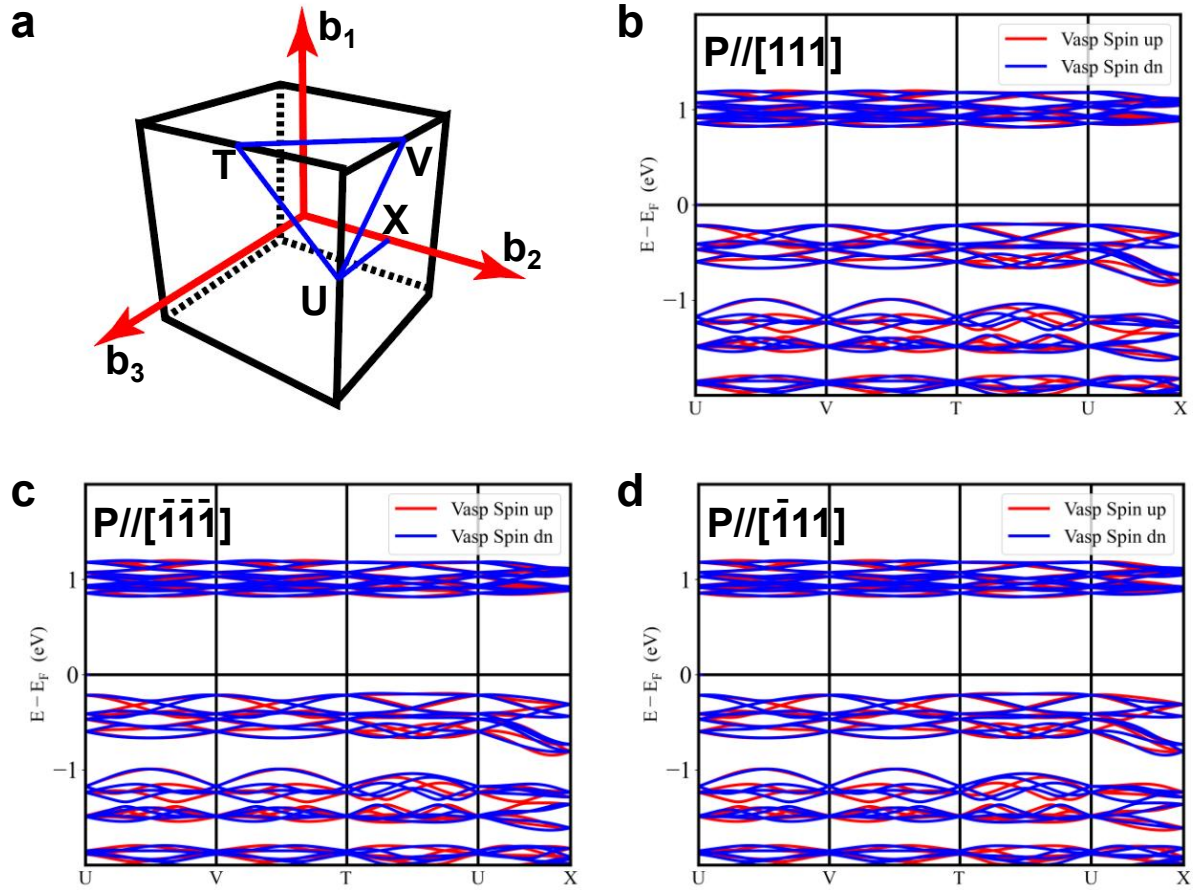
Extended Data Fig. 1. BFO band structure. a, First Brillouin zone of BFO. The high symmetric points are highlighted. **b-d,** First-principle calculated band structures for BFO with the ferroelectric polarization $\mathbf{P}$ pointing along [111] (**b**), [$\bar{1}\bar{1}\bar{1}$] (**c**) and [$\bar{1}11$] (**d**) directions, respectively.
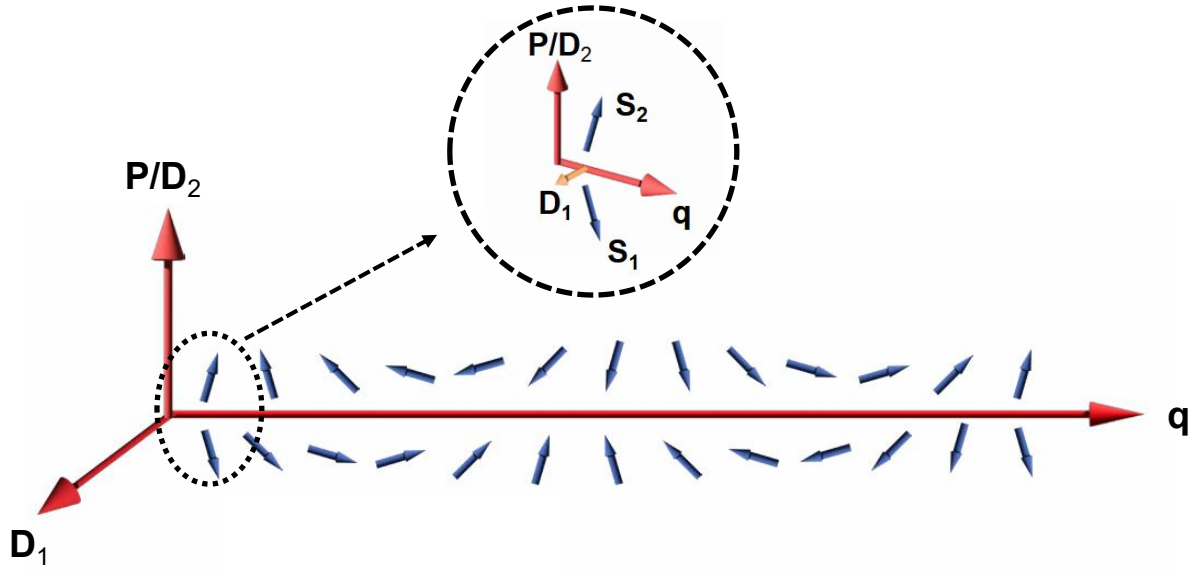
Extended Data Fig. 2. **The antiferromagnetic order of BFO.** A sketch of spin cycloid that propagates along $\mathbf{q}= [1\bar{1}0]$. Ferroelectric polarization $\mathbf{P}$ points along [111], while $\mathbf{D}_1$ and $\mathbf{D}_2$ represent homogeneous and inhomogeneous DMI, respectively, with $\mathbf{D}_2 \parallel \mathbf{P}$, $\mathbf{D}_2 \perp \mathbf{q}$, and $\mathbf{D}_1 \parallel \mathbf{S}_1 \times \mathbf{S}_2$.
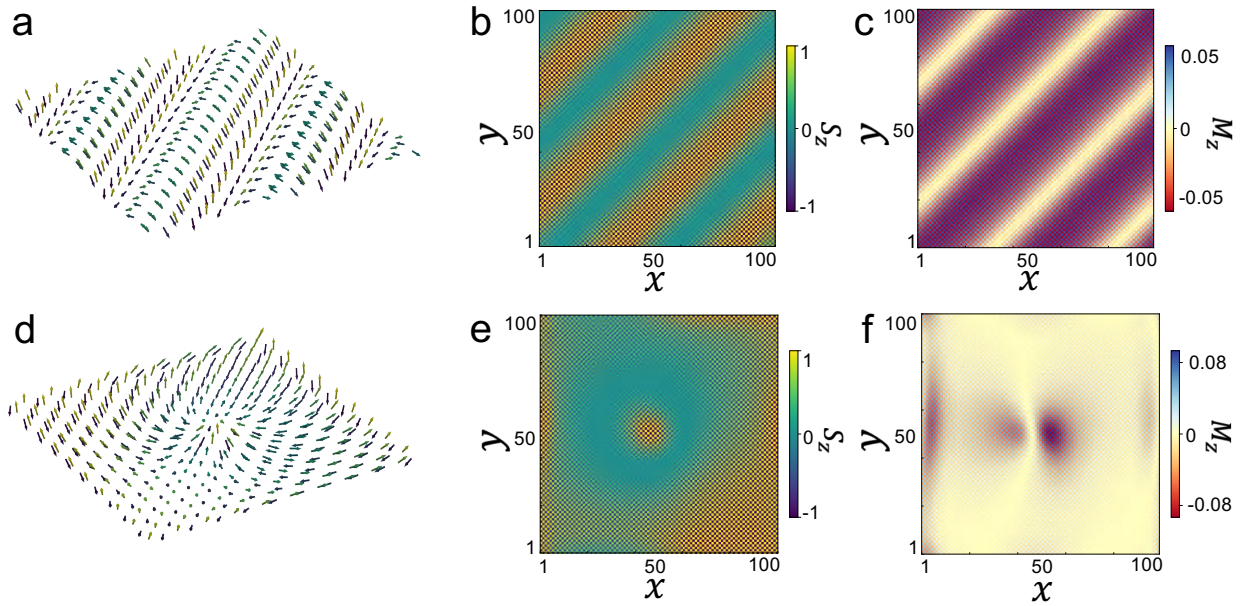
Extended Data Fig. 3. **Spin cycloid ground state and skyrmion state in BFO.** Three-dimensional plot (**a,d**), two-dimensional colormap (**b,e**) and the weak magnetization (**c,f**) between canted antiparallel spins on neighboring sites for the spin-cycloid ground state (**a-c**) and the Néel skyrmion state (**d-f**) in BFO. Here, the arrows in (**a,d**) represent the local spin direction while the color indicates S_z value. Only 1 out of 25 (5×5) spin vectors is plotted in (**a,d**) for clarity.
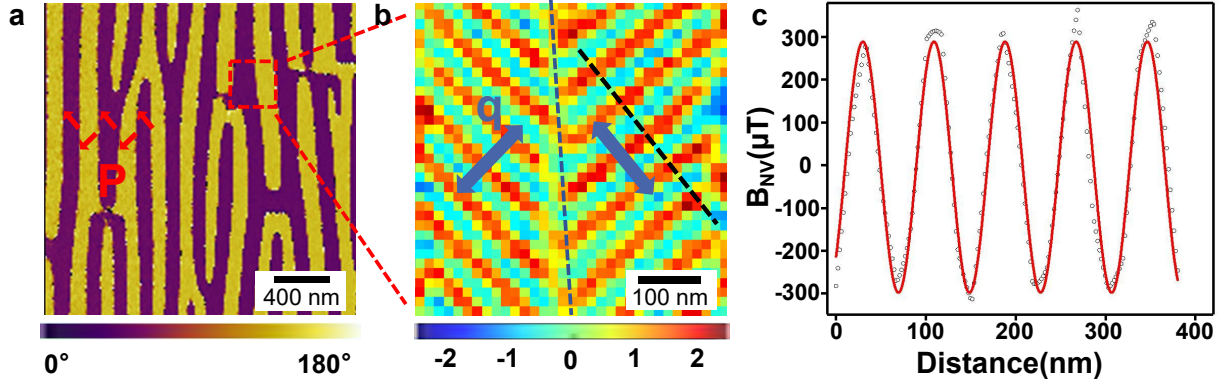
Extended Data Fig. 4. Magnetoelectric coupling in BFO. a, Lateral piezoresponse force microscopy (LPFM) image of a ~ 100nm BFO film with $71°$ DWs grown on a (110) oriented DSO substrates. The red arrows indicate the in-plane projection of the ferroelectric polarization vector. **b,** Corresponding magnetic field distributions recorded from the dashed-red areas of the LPFM (**a**,) with the scanning-NV magnetometer (SNVM) operating in Full-B imaging mode. The blue arrow indicates the direction of **q** propagation. The scalebars in (**a**) and (**b**) are 400 nm and 100 nm, respectively. **a** Linecuts of the magnetic field distribution along the cycloid propagation direction (black dashed line in **b**).
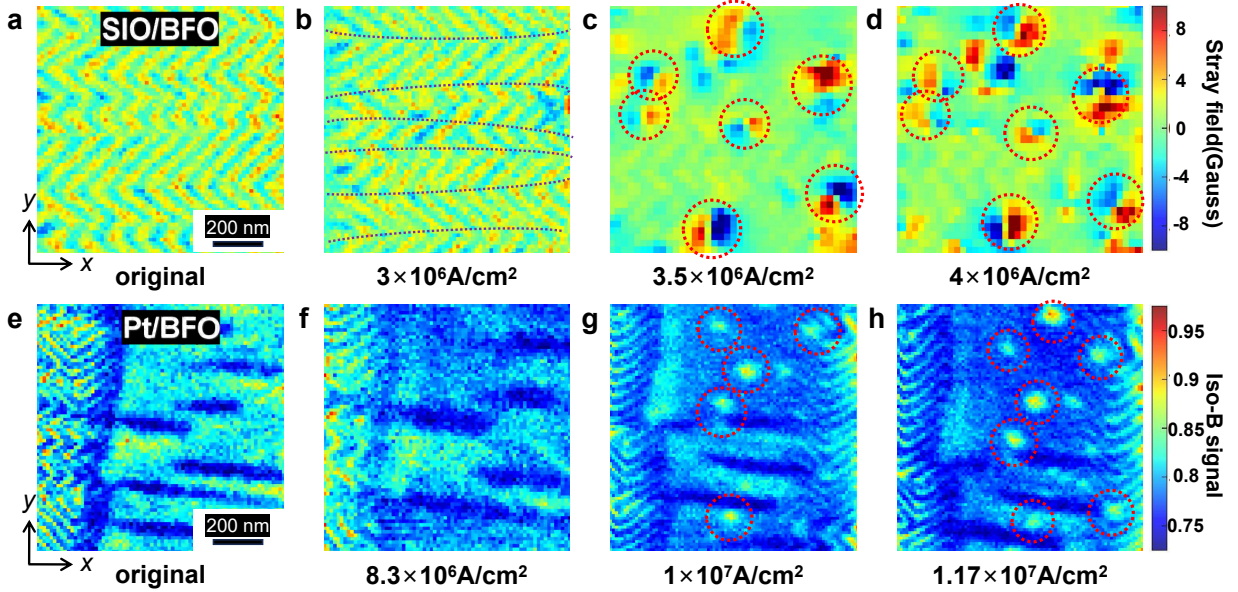

Extended Data Fig. 5. Experimental study on pulse current regulation of BFO with different top electrodes a, SNVM images of magnetic domains in SIO/BFO under applied pulsed current densities , showing the transformation of spin cycloids to skyrmions at $\sim 3.5 \times 10^6$ A/cm^2. **e-h** The corresponding applied current density J_s is at $\sim 1 \times 10^7$ A/cm^2 for the top electrodes Pt/BFO. The scalebar in **a-h** is 200 nm.
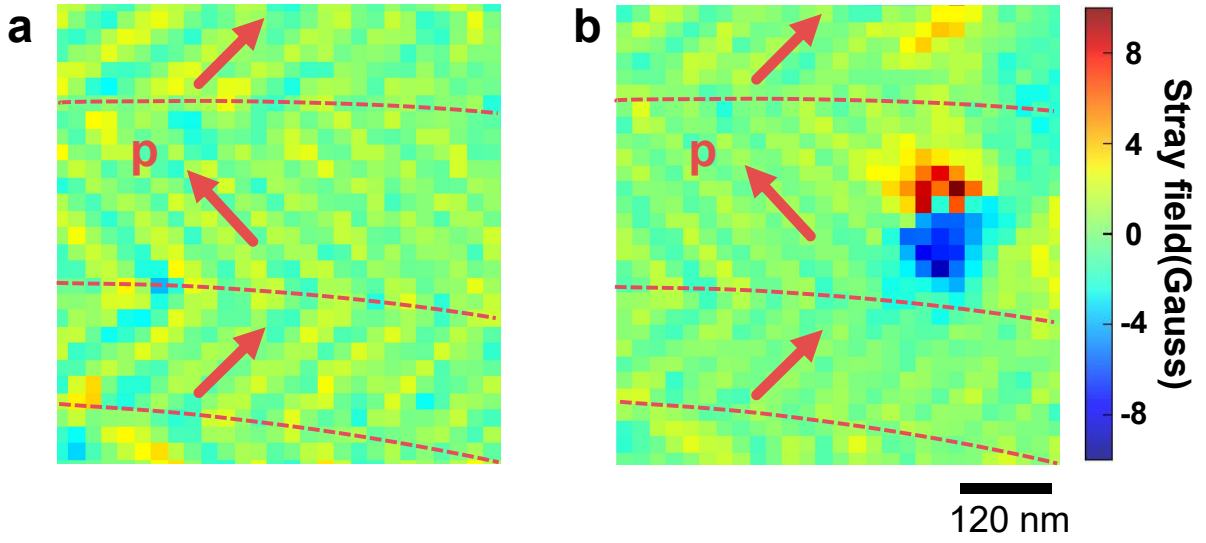
Extended Data Fig. 6. Experimental study on electric polarization of BFO via SNVM. a, b, SNVM images show the pulsed-current-driven transformation of magnetic domains in SIO/BFO. The red arrows indicate the in-plane projection of the ferroelectric polarization vector. The red dashed lines indicate the domain boundaries.
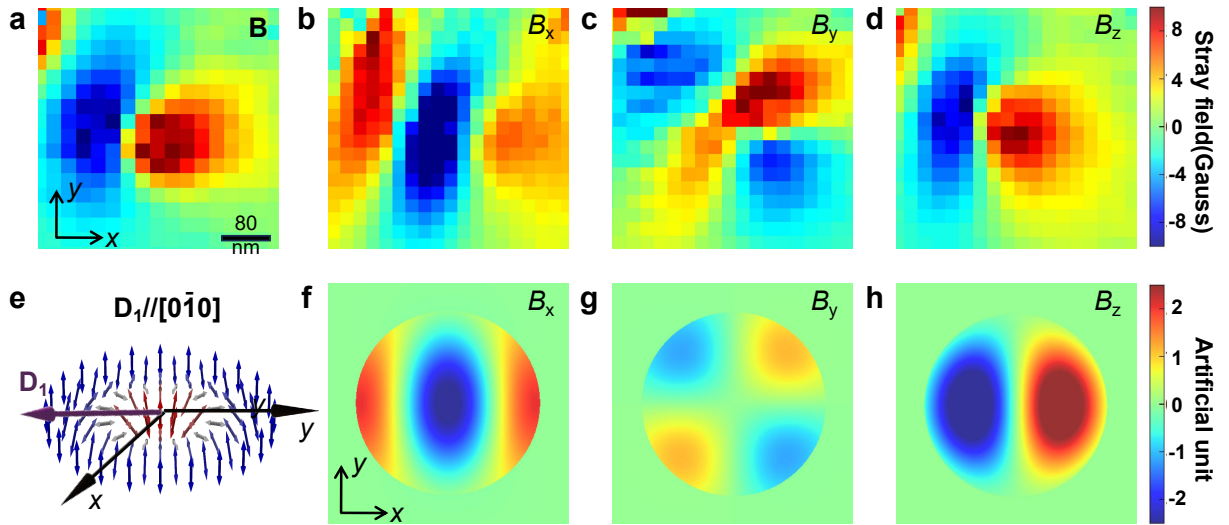

Extended Data Fig. 7. Control of skyrmions by ferroelectric polarization a, Various skyrmion phases, with DMI direction modulated by ferroelectric polarization. **b-d,** Stray field components reconstructed along the x, y, and z directions based on panel **a**. **e,** Simulated configuration of a skyrmion with DMI direction along [010]. **f-h,** Stray field distributions for the simulated skyrmion in **e** along the x, y, and z directions, respectively.
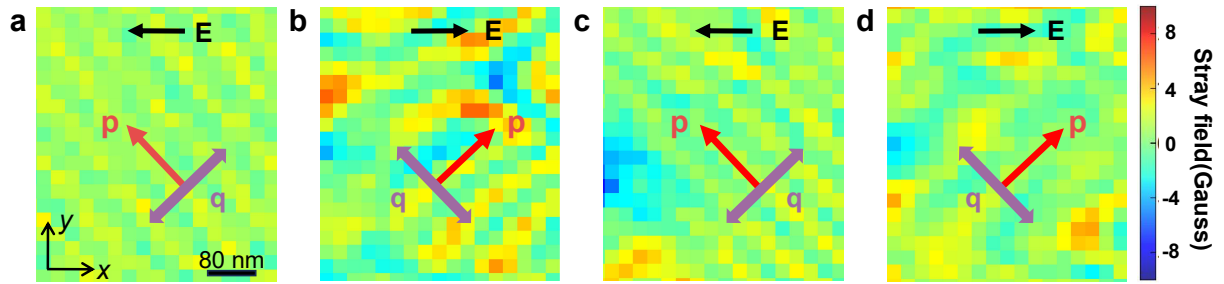
Extended Data Fig. 8. Electrical control of the spin cycloid. a-d SNVM images of spin cycloid under E= -300 kV/cm (**a,c**) and E= 300 kV/cm (**b,d**),respectively. The polarization **P** align parallel to the directions marked by the red arrows in each panel, flipping by 90° under the electric field shown in (**a,c**) and (**b,d**). The purple arrows indicate the directions of **q** propagation, which are perpendicular to **P** directions.
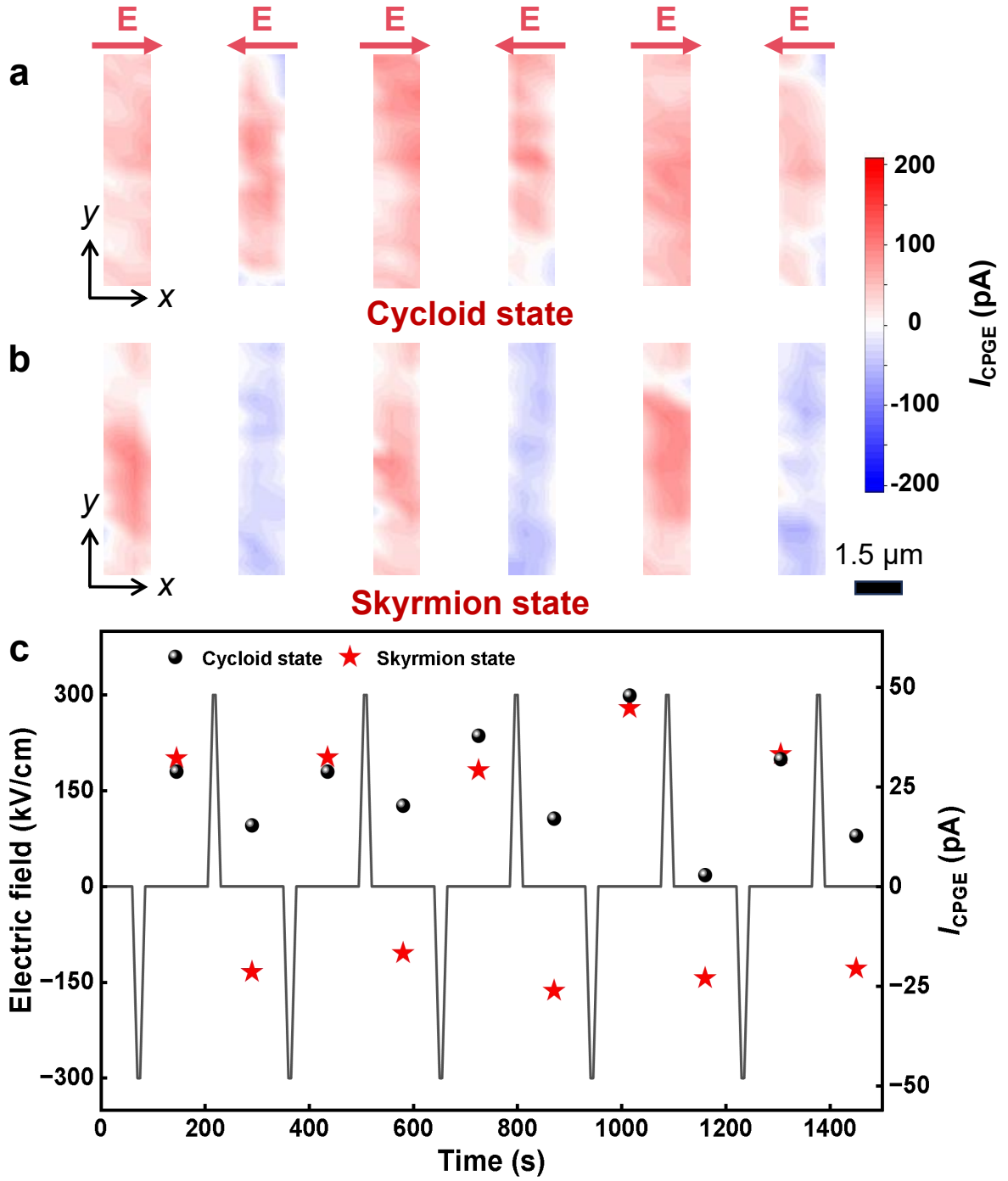
Extended Data Fig. 9. Responses of the spin photocurrent (I_{CPGE}) to electric-field modulation in cycloid and skyrmion states within the BFO system. a,b, Mapping diagrams of the I_{CPGE} under electric-field modulation for the cycloid and skyrmion states, respectively. **c,** Black spheres and red asterisks denote the magnitudes of the overall average I_{CPGE} within the region of (**a**) and (**b**), respectively. For the cycloid state, the I_{CPGE} remains positive during the application of both positive and negative electric fields. Conversely, in the skyrmion state, the magnitude of the I_{CPGE} undergoes a regular transition in positive-negative polarity under electric-field modulation. The color bar indicates the magnitude of spin photocurrent in pA, and the scale bar is 1.5 μm.
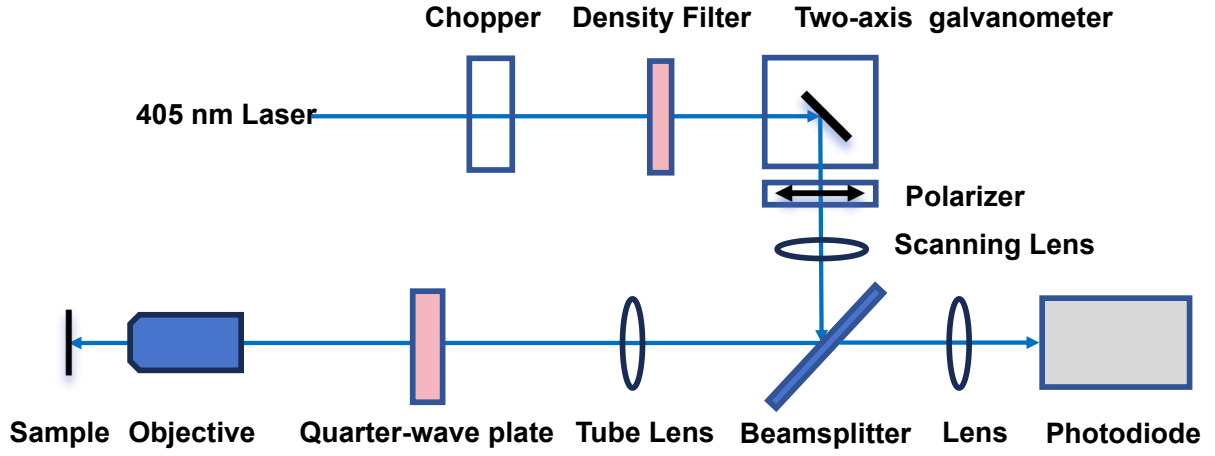
Extended Data Fig. 10. Schematic figure for the optical measurement setup of the spin photocurrent measurement system. A 405 nm laser spot was focused on the sample, with its polarization state tuned by a quarter-wave plate for circular polarization, and scanned using a two-axis galvanometer for photocurrent mapping.
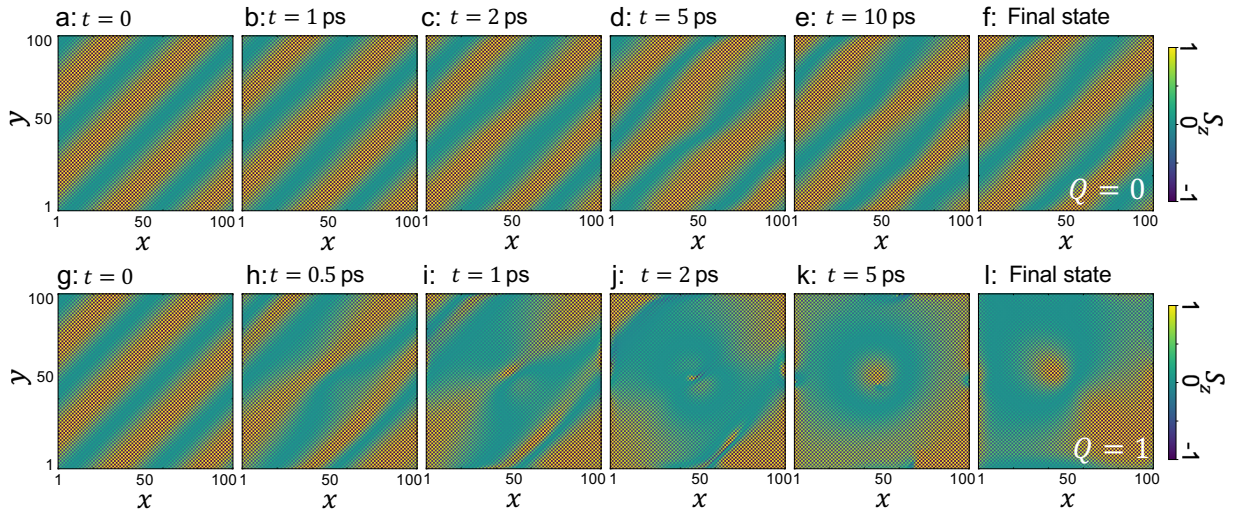
Extended Data Fig. 11. Skyrmion nucleation in BFO via spin-orbit torque. Time evolutions of the spin cycloid ground state at five representative time labeled ontop of each figure, and the final spin state after sufficient relaxation for BFO under a 10ps spin orbit torque of magnitude $J_c = 1.0 \times 10^6 \mathrm{A} \cdot \mathrm{cm}^{-2}$ (**a-f**) and $J_c = 1.1 \times 10^7 \mathrm{A} \cdot \mathrm{cm}^{-2}$ (**g-l**), respectively. The Néel order topological charge for the final states in (**f**) and (**l**) are $Q = 0$ and $Q = 1$.
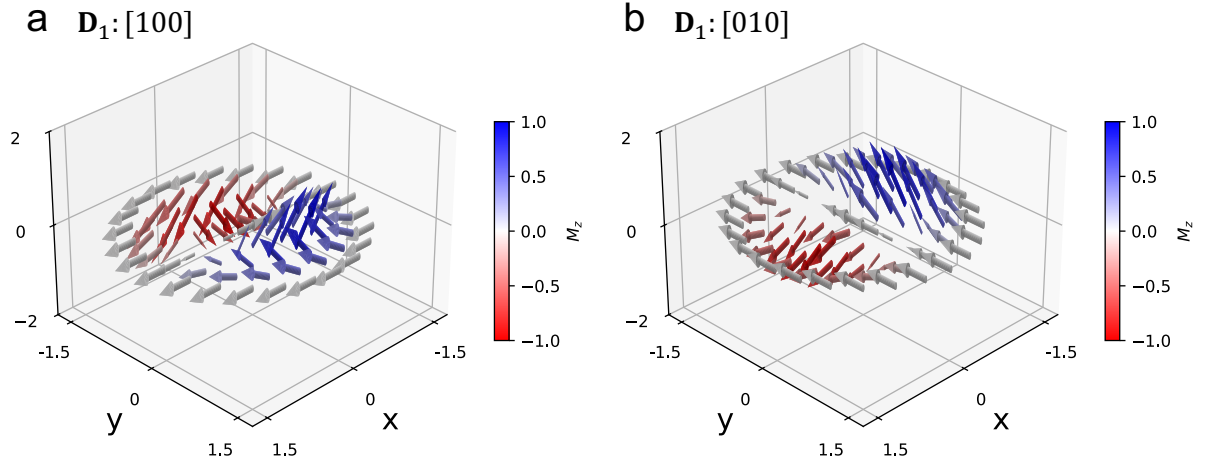
Extended Data Fig. 12. **Canted moments for BFO skyrmion with different** D_1**. a,** D_1 aligns along [100]. **b,** D_1 aligns along [010].